# Image Segmentation Based on the Hybrid Bias Field Correction

**Zhi-Feng Pang · Zhenyan Guan · Yue Li · Ke Chen, H Ge**

**Abstract**. Image segmentation is the foundation for analyzing and understanding high-level images. How to effectively segment an intensity inhomogeneous image into several meaningful regions in terms of human visual perception and ensure that the segmented regions are consistent at different resolutions is still a very challenging task. In order to describe the structure information of the intensity inhomogeneous efficiently, this paper proposes a novel hybrid bias field correction model by decoupling the multiplicative bias field and the additive bias field. These kinds of bias fields are assumed to be smooth, so can employ the Sobolev space to feature them and use a constraint to the multiplicative bias field. Since the proposed model is a constrained optimization problem, we use the Lagrangian multiplier method to transform it into an unconstrained optimization problem, and then the alternating direction method can be used to solve it. In addition, we also discuss some mathematical properties of our proposed model and algorithm. Numerical experiments on the natural images and the medical images demonstrate performance improvement over several state-of-the-art models.

**Keywords** Image segmentation · Bias correction · Intensity inhomogeneity · Augmented Lagrangian method · MRI

## 1 Introduction

Medical image segmentation is a perfect combination of the medical field and computer vision field, and it is the basis of various medical image applications. The purpose of medical image segmentation is to separate the parts with special meaning in medical images, these regions have similar properties such as grayscale, texture, brightness, contrast, etc[2]. Due to the factors such as space and imaging equipment illumination, the problem of uneven pixel intensity often occurs, which poses a great challenge to image segmentation. Intensity inhomogeneity is a smoothly varying bias field. For instance, in magnetic resonance imaging (MRI), intensity inhomogeneity can lead to inconsistency of pixels in the same tissue [28].

During these decades, there has been a lot of research on image segmentation[21, 19, 26, 32]. Various variational methods, partial differential equations, and deep learning segmentation methods have been proposed for image processing and image segmentation [11, 14, 16, 22]. There are two major classical methods for image segmentation: region-based models and edge-based models. Region-based segmentation methods utilize region information to guide the evolution of initial contours. Chan-Vese (CV) model [5], local binary fitted (LBF) model [15] and local intensity clustering (LIC) model [16] are the approaches of region-based models. In edge-based segmentation methods, the segmentation process is performed by evolving the initial contour to the target boundary. Snake model [13], Geodesic active contours model [4] are the classical edge-based models. However, these methods are greatly affected by the initial contour and the boundary of the target object, and curve evolution tends to fall to a local minimum. These models

College of Mathematics and Statics, Henan University, Kaifeng, China.

are based on the assumption that the gray distribution is uniform. Therefore, it cannot achieve a good segmentation effect for images with intensity inhomogeneity. It is a challenging task to segment regions of interest from images with inhomogeneous intensity. To this end, a lot of research has been done on the problem of image segmentation with uneven gray levels[25, 19, 20, 17].

Intensity inhomogeneity (i.e. bias field) is present in many real-world images from different modalities, such as X-ray/tomography and magnetic resonance (MR) images. This phenomenon also occurs in natural images, mostly due to uneven lighting. To solve the image segmentation problem of intensity inhomogeneity, Chan and Vese [29] proposed a piecewise smooth (PS) model. This method uses the piecewise smooth function to replace the gray constant value function, and effectively segment the image with intensity inhomogeneity. However, this model requires periodic initialization, which is difficult to apply and cannot be generalized. Despite the advantages of these level set-based methods, the solution can easily get stuck in local minima, depending on the initialization. Li et al. [16] introduced the kernel function to the active contour model and then proposed the LBF model. This model solves the level set reinitialization problem to a certain extent. In the literature [16], the author introduced a bias field into the segmentation model, completes the bias field correction at the same time as the segmentation, and improves the model's dependence on the initial contour. Zhang et al.[36] presented a novel level set method for image segmentation in the presence of intensity inhomogeneity. Simultaneously, Duan et al. [7] introduced an $L_0$ gradient regularizer to model the true intensity and a smooth regularizer to model the bias field. Ali et al. [1] proposed a variational model with hybrid images data fitting energies for segmentation, this method achieves good results on images with intensity inhomogeneity. Niu et al. [24] improved Li's model by introducing local entropy, which redefined the energy function of the level set as a weighted energy integral. Jung [12] proposed a piecewise-smooth image segmentation model (L1PS) by introducing $L_1$ Data-Fidelity Terms. This model can effectively deal with the image with intensity inhomogeneity and noise. In [38], Zosso et al. proposed the CVB model based on Retinex theory, which assumes that a natural image can be seen as the sum of illuminance bias part and reflectance. Subudhi et al. [27] proposed a fuzzy set based on Gibbs Markov Random Field (MRF) to model the spatial background information of magnetic resonance imaging, and combined with the principle of maximum posterior probability estimation to segment images with uneven illumination. Yu et al. [35] proposed an edge-based active contour model (ACM) for medical image segmentation, which integrates adaptive perturbation into the framework of edge-based ACM. Thus, the stability of the evolution curve and the accuracy of numerical calculation are ensured. Memon et al. [20] proposed a region-based hybrid active contour model. The weight function in the model can obtain smooth contour boundaries at different intensity levels, suppress the evolution of false contours, and regularize the target boundaries. In the literature[3], Alirr et al. utilized deep learning and level set methods for organ segmentation. In this article, we consider the total variation method to segment the kidney and spleen. Weng et al.[33] proposed a level set method based on additive bias correction for image segmentation with intensity inhomogeneity. Due to the different intensity values of image objects, this method is not suitable for segmenting objects with significantly multiple colors.

In the ideal case, the physical property of the background area of the real image is zeros pixels in MRI. Therefore, we assume that the input image consists of two parts, one is the product of the piecewise constant function and the multiplicative bias field, and the other is the additive bias field. This method makes full use of the advantages of decomposing the image into two parts, namely the true image, which characterizes the physical properties of the image, and the multiplicative bias field, which reflects the intensity inhomogeneity, and its respective spatial properties and additive bias field. Bias field estimation and target segmentation are energy minimization processes implemented simultaneously. Based on the augmented Lagrangian function, we design a fast and effective optimization method to solve the problem and provide theoretical analysis to ensure the existence of the model solution and the local convergence of the algorithm. Extensive experiments on natural images and real medical images show that the proposed segmentation model outperforms state-of-the-art methods in terms of robustness to noise and segmentation accuracy.

The framework of this paper is as follows: Section 2 mainly introduces the proposed model with multiplicative and additive bias field correction and establish the existence of a solution. We also review several variational segmentation models related to our model in section 2. We propose an optimization algorithm for solving this model using the variable splitting scheme and augmented Lagrangian method in section 3. In section 4, we conduct related experiments and analysis on natural images and MRI images respectively. Then, we present the numerical results of our model and compare the performance with other existing methods. Finally, in Section 5 conclusions of this work are drawn.

## 2 Related work

Throughout this paper, let $\Omega \subset R^2$ be an open and bounded image domain, and $I : \Omega \to \Re$ be an observed grayscale image to be segmented. Let $\mathcal{C}$ be the edge set in $\Omega$. The purpose of segmentation is to divide the image domain $\Omega$ into $N$ disjoint parts $\{\Omega_i\}_{i=1}^N$, such that $\Omega = \cup_{i=1}^N \Omega_i \cup \mathcal{C}$. i.e. $\Omega_i \cap \Omega_j = \emptyset$, $\forall i \neq j$ .

### 2.1 Related variational model

In the literature [23], For an observed image $I$, to find optimal piecewise sooth approximation $I_0 : \mathrm{x} \in \Omega \to \mathbb{R}$, $\mathcal{C}$ be a closed contour. The Mumford-Shah(MS) model can be represented as the following minimization problem

$$E_{MS}(I_0, \mathcal{C}) = \frac{\lambda}{2} \int_\Omega (I - I_0)^2 \mathrm{dx} + \int_{\Omega/\mathcal{C}} |\nabla I_0|^2 \mathrm{dx} + \nu |\mathcal{C}|. \tag{1}$$

where $\lambda, \nu$ are the positive weight parameters, and $|\mathcal{C}|$ represents the total length of the arcs making up $\mathcal{C}$. Here $I_0$ is the piecewise smooth approximation function of image $I$. The three terms of the model are explained as follows: the first term requires $I_0$ to be approximately $I$; the second term requires $I_0$ to vary little in each region $\Omega_i$; the third term requires the boundary contour $\mathcal{C}$ to be as short as possible. Since the discontinuity of the integral region in the latter two terms and the non-convexity of the MS model, it is difficult to realize the numerical minimization problem. Then there are some techniques to improve the MS model. Chan and Vese [5] proposed the minimization energy function by simplifying the MS model

$$E_{CV}(\phi, c_1, c_2) = \int_\Omega (I - c_1)^2 H(\phi) + (I - c_2)^2 (1 - H(\phi)) \mathrm{dx} + \nu \int_\Omega |\nabla H(\phi)| \mathrm{dx}. \tag{2}$$

where $H$ is Heaviside function, $\phi$ is the level set function, and the contour $\mathcal{C} = \{\mathrm{x} : \phi(\mathrm{x}) = 0\}$. The minimization problem (2) is to find constant approximations $c_1$ and $c_2$ of the mean intensity of pixels inside and outside the contour $\mathcal{C}$ of the image $I$ to be segmented. Since the model (2) is non-convex, Chan [6] uses a convex relaxation technique by $u := H(\phi)$ to transform it into a convex problem.

$$\min_{u \in [0,1]} \int_\Omega (I - c_1)^2 u + (I - c_2)^2 (1 - u) \mathrm{dx} + \nu \int_\Omega |\nabla u| \mathrm{dx}. \tag{3}$$

However, these models have segmentation errors when dealing with the image with intensity inhomogeneity. In the literature [8], Gao et al. introduced a local modified about (2) model to process the image with intensity inhomogeneity. However, for images with serious intensity inhomogeneity, or in the presence of noise, we still need to conduct further research.


**Fig. 1** Image decomposition assumptions about intensity inhomogenetity. $I$ is the observed image. $J$ is the true image. $b_1$, $b_2$ are bias field.

### 2.2 Image model

In [10], Horn et al. analyzed the illumination problem and proposed the multiplicative model of observed image, which describe the composition of real-world images. The real image can be represented as a method of synthesizing the image model. For an observed image $I$ can consist of reflectance portion, illumination portion and additive noise. It can be expressed as the following formula

$$I = bJ + n. \tag{4}$$

where $J$ represents the intrinsic physical characteristics of the observed image, it's called a true image. The bias field is represented as $b$, which is the component with uneven intensity. Assumed that $n$ is the zero-mean Gaussian noise. This model has been widely used in modeling images with intensity inhomogeneity. The assumptions regarding the true image and bias field are as follows

- The bias field $b$ is assumed to vary slowly and smoothly. Thus, the bias field $b$ is approximately constant within the neighborhood of each point in the image domain.
- The image domain $\Omega$ is divided into disjoint $N$ parts. The true image $J$ takes $N$ different constant values $c_1, \cdots, c_N$ in each disjoint field.

In this article, we consider that the observed image consists of an illuminated part and a reflected part. But we assume that the part where the intensity is inhomogeneity is made up of two parts, which is $b = \{b_1, b_2\}$. Here we refer to the smoothing term of the multiplicative bias field and the smoothing term of the additive bias field, respectively. The bias field $b_1$ is the multiplicative component of intensity inhomogeneity, $b_2$ is the additive component of intensity inhomogeneity, and assume that $n$ is zero-mean Gaussian noise. The novel synthesizing image model can be expressed as the following formula

$$I = b_1 J + b_2 + n. \tag{5}$$

According to the bias correction assumption in the formula (4), this paper introduces two different bias fields into the processing of uneven intensity. We make the following assumptions regarding the true image $J$ and bias field $b_1, b_2$.

- The bias fields $b_1, b_2$ are slowly varying and smoothly, and we assume that the bias fields $b_1$ and $b_2$ are approximately constant within the neighborhood of each point in the image domain.
- The image domain $\Omega$ is divided into disjoint $N$ parts, each part is approximately a constant value $c_i$ $(i = 1, \cdots, N)$, respectively. The true image $J$ takes $N$ different constant values $c_1, \cdots, c_N$ in each disjoint field $\Omega_1, \cdots, \Omega_N$.

Based on the synthesizing image model, we define $b_1$ and $b_2$ are multiplicative bias field and additive bias field. Here, we temporarily ignore the noise part of the observed image. Then the formula (5) can be represented by Fig. 1. The multiplicative and additive bias field are displayed in the form of an image.

2.3 Variational framework and Bias field correction

Assume that the observed image $I$ consists of the product of a piecewise smooth function $c_i$ ($i = 1, 2.$) and a multiplicative bias field $b_1$ and an additive bias field $b_2$. We penalize the smooth function multiplicative bias field $b_1$ by imposing a constraint such that $b_1$ is a bias field that varies smoothly around a constant value. Then, we propose the following segmentation model to process the images with intensity inhomogeneity.

$$\begin{aligned}\min_{u,b_1,b_2,c_1,c_2} \lambda &\int_\Omega (I - b_1c_1 - b_2)^2 u + (I - b_1c_2 - b_2)^2(1-u)\mathrm{dx} \\ &+ \alpha \int_\Omega |\nabla b_1|^2 \mathrm{dx} + \beta \int_\Omega |\nabla b_2|^2 \mathrm{dx} + \int_\Omega |\nabla u| \mathrm{dx}, \\ \text{s.t.} \quad &\int_\Omega (b_1 - 1)^2 \mathrm{dx} \le \varepsilon, \quad u \in \{0, 1\}.\end{aligned} \tag{6}$$

where $\varepsilon > 0$ is the bias parameter, $\lambda, \alpha, \beta$ are the weight parameters, and $u$ subject to the constraint $\{0, 1\}$. In the right side of (6), the first term is the data fitting term, which forces $b_1c_i + b_2, i = 1, 2.$ to be close to the input image $I$, the second term and the third term are smooth term of bias field, which ask that bias fields vary smoothly. The last term is the length term to regularize the contour. Our goal is to recover $b_i, c_i, i = 1, 2.$ from the observed image $I$ and obtain the segmentation result. The bias field $b_1$ is usually assumed to vary slowly and take a value around 1, so we use constraint terms in the model to represent it.

Since the model (6) is non-convex due to the binary constraint, and it is hard to solve numerically. Therefore, we convex relaxation of $u$, such that $u \in [0, 1]$. Transform the formula (6) into an unconstrained optimization problem, and the corresponding optimization problem is

$$\begin{aligned}\min_{u,b_1,b_2,c_1,c_2} E(u, b_1, b_2, c_1, c_2) :=& \lambda \int_\Omega (I - b_1c_1 - b_2)^2 u + (I - b_1c_2 - b_2)^2(1-u)\mathrm{dx} + \alpha \int_\Omega |\nabla b_1|^2 \mathrm{dx} \\ &+ \beta \int_\Omega |\nabla b_2|^2 \mathrm{dx} + \int_\Omega |\nabla u| \mathrm{dx} + \nu \int_\Omega (b_1 - 1)^2 \mathrm{dx} + \Gamma_{\mathcal{D}}(u).\end{aligned} \tag{7}$$

where $\nu > 0$ is penalty parameter. $\Gamma_{\mathcal{D}}(u)$ is the characteristic function can be written as

$$\Gamma_{\mathcal{D}}(u) = \begin{cases} 0, & \text{if } u \in \mathcal{D}, \\ +\infty, & \text{otherwise.} \end{cases}$$

where $\mathcal{D} = [0, 1]$.

2.4 Convergence analysis

Before the theoretical analysis, we first introduce some related lemmas, such as the lower semi-continuity, the definition of bounded variation space, and Poincare inequality[30]. Then we prove the convergence of the optimal solution.

**Lemma 1.** Assumed that $u \in L^1(\Omega)$, according to the following equality, we define the bounded variation space $BV(\Omega)$ as a space

$$\int_\Omega |Du| := \sup \left\{ \int_\Omega u \mathrm{div}(\phi) \mathrm{dx} | \phi \in C_0^1(\Omega; \mathbb{R}^n), |\phi| \le 1 \right\}.$$

is finite. Then the $BV$ norm is defined in $BV(\Omega)$ space can be written as

$$\|u\|_{BV} = \|u\|_{L^1(\Omega)} + \int_\Omega |Du|.$$

The $BV(\Omega)$ space is a Banach space under the $BV$ norm. The $BV(\Omega)$ space allows functions to have discontinuous properties. Therefore, piecewise constant or smooth images are usually assumed in the $BV(\Omega)$ space[18]. The term $\int_\Omega |Du|$ is represent total variation of $u$. Total variational regularization is popular in variational image modeling.

**Lemma 2.** Supposed that $u_j \in BV(\Omega)(j = 1, \ldots)$ and $u_j \to u$ in $L^1_{loc}(\Omega)$. Then

$$\int_\Omega |Du| \leq \liminf_{j\to\infty} \int_\Omega |Du_j|.$$

**Lemma 3.** Let $\Omega$ be a bounded open subset of an n-dimensional Euclidean space with a Lipschitz boundary, then there exists a constant $C$, whose value depends only on $\Omega$ and $p$. For each function $u$ in Sobolev space $W^{1,p}(\Omega)$, denoting $(u)_\Omega := \dfrac{1}{|\Omega|}\displaystyle\int_\Omega u\mathrm{dx}$, The Poincare inequality is defined as

$$\|u - (u)_\Omega\|_{L^p(\Omega)} \leq C\|\nabla u\|_{L^p(\Omega)}.$$

where $1 \leq p \leq n$.

**Lemma 4.** Let $\Omega$ be a measure space, and $u_j$(j=1,...) be a sequence of measurable positive functions with real values, such that

$$\int_\Omega \liminf_{j\to\infty} u_j\mathrm{dx} \leq \liminf_{j\to\infty} \int_\Omega u_j\mathrm{dx}.$$

where the limit of the function is the limit in the sense of point by point convergence.

**Theorem 1.** Let $I \in BV(\Omega)$, $c_1, c_2 > 0$, and the admissible set is $\Lambda = \{u, b_1, b_2 | u \in BV(\Omega), \text{satifies}\, u \in [0,1], b_1 \in W^{1,2}(\Omega), b_2 \in W^{1,2}(\Omega)\}$. For fixed parameters $\lambda, \alpha, \beta$ are positive, there exists a minimizer $(u^*, b_1^*, b_2^*, c_1^*, c_2^*)$ of problem (7) in the admissible set $\Lambda$.

**Proof.** It is obvious that every term in (7) is positive, it has a finite lower bound. Thus there exits a constant $K$, we have the following inequality

$$\inf E(u, b_1, b_2, c_1, c_2) \leq K. \tag{8}$$

according to the definition of the lower bound, hence there exits a minimizing sequence $(u^k, b_1^k, b_2^k, c_1^k, c_2^k)$, such that

$$\lim_{k\to\infty} E(u^k, b_1^k, b_2^k, c_1^k, c_2^k) = \inf E(u, b_1, b_2, c_1, c_2). \tag{9}$$

For the sequence $\{u^k\}$, notice that $\Omega \in \mathbb{R}^2$ be a bounded image domain, we have $\int_\Omega u^k\mathrm{dx} \leq |\Omega|$ due to $u \in \mathcal{D}$. And $u^k \in BV(\Omega) \hookrightarrow L^2(\Omega)$, hence there exits $u^* \in BV(\Omega)$, such that

$$u^k \xrightarrow[L_1(\Omega)]{} u^* \quad \text{and} \quad u^k \xrightarrow[\text{a.e. in } \Omega]{} u^*. \tag{10}$$

By the weak lower continuous of TV semi-norm, we obtain the following inequality of the problem

$$\int_\Omega |\nabla u^*|\mathrm{dx} \leq \liminf_{k\to\infty} \int_\Omega |\nabla u^k|\mathrm{dx}. \tag{11}$$

For the sequence $\{b_i^k\}$, where $i = 1, 2$. Let $(b_i^k)_\Omega := \frac{1}{|\Omega|}\int_\Omega b_i^k\mathrm{dx}$ donate the mean value in $\Omega$. By the Poincare inequality, it follows that there exists a constant $C > 0$, such that

$$\begin{aligned} \|b_i^k\|_{L^2(\Omega)} &= \|b_i^k - (b_i^k)_\Omega + (b_i^k)_\Omega\|_{L^2(\Omega)} \leq \|b_i^k - (b_i^k)_\Omega\|_{L^2(\Omega)} + \|(b_i^k)_\Omega\|_{L^2(\Omega)} \\ &\leq C\|b_i^k - (b_i^k)_\Omega\|_{L^2(\Omega)} \leq C\|\nabla b_i^k\|_{L^2(\Omega)} \leq CK. \end{aligned} \tag{12}$$

and therefore, the sequences $\{b_i^k\}$ and $\{\nabla b_i^k\}$ are bounded in the space $W^{1,2}(\Omega)$, we have the following inequality

$$\int_\Omega |\nabla b_i^*|^2\mathrm{dx} \leq \liminf_{k\to\infty} \int_\Omega |\nabla b_i^k|^2\mathrm{dx}, \;\; i = 1, 2. \tag{13}$$

and the sequence $\{b_1^k\}$ is given by

$$\int_\Omega (b_1^* - 1)^2 \mathrm{d}x = \liminf_{k\to\infty} \int_\Omega (b_1^k - 1)^2 \mathrm{d}x. \tag{14}$$

For the sequence $\{c_i^k\}$, where $i = 1, 2$. $c_i$ is bound in $\mathbb{R}$. Then there exits a convergent subsequence, thus we have $c_i^k \to c_i^*$. According to $u^k \to u^*$, $b_i^k \to b^*$, and $c_i^k \to c_i^*$, based on the Fatou lemma we get

$$\int_\Omega \liminf_{k\to\infty} (I - c_1^k b_1^k - b_2^k)^2 u^k \mathrm{d}x = \int_\Omega (I - c_1^* b_1^* - b_2^*)^2 u^* \mathrm{d}x \le \liminf_{k\to\infty} \int_\Omega (I - c_1^k b_1^k - b_2^k)^2 u^k \mathrm{d}x. \tag{15}$$

$$\int_\Omega \liminf_{k\to\infty} (I - c_2^k b_1^k - b_2^k)^2 u^k \mathrm{d}x = \int_\Omega (I - c_2^* b_1^* - b_2^*)^2 u^* \mathrm{d}x \le \liminf_{k\to\infty} \int_\Omega (I - c_2^k b_1^k - b_2^k)^2 u^k \mathrm{d}x. \tag{16}$$

Thus we obtain the following inequality

$$E(u^*, b_1^*, b_2^*, c_1^*, c_2^*) \le \liminf_{k\to\infty} E(u^k, b_1^k, b_2^k, c_1^k, c_2^k) = \inf E(u, b_1, b_2, c_1, c_2). \tag{17}$$

To summarize, we prove that $(u^*, b_1^*, b_2^*, c_1^*, c_2^*)$ is a solution of the problem (7).

## 3 Numerical algorithm

We first solve the subproblem of $u$, and then solve the other variables separately. Let's introduce two auxiliary variables $p_1, p_2$ to transform (7) into the following constrained optimization problem. The solution method is to transform the original optimization problem into an alternate-direction optimization multiplier method by variable splitting. So far, the problem that we consider is therefore

$$\begin{aligned} \min_{u,b_1,b_2,c_1,c_2} \lambda \int_\Omega p_1^2 u + p_2^2 (1-u) \mathrm{d}x + \alpha \int_\Omega |\nabla b_1|^2 \mathrm{d}x + \beta \int_\Omega |\nabla b_2|^2 \mathrm{d}x \\ + \int_\Omega |\nabla u| \mathrm{d}x + \nu \int_\Omega (b_1 - 1)^2 \mathrm{d}x + \Gamma_{\mathcal{D}}(u), \\ \text{s.t.} \quad p_1 = I - b_1 c_1 - b_2,\ p_2 = I - b_1 c_2 - b_2. \end{aligned} \tag{18}$$

### 3.1 The $u$-subproblem

By introducing the auxiliary variable $\mathbf{q} = \nabla u$, and the corresponding optimization problem is

$$\begin{aligned} \min_{u\in[0,1]} \lambda \int_\Omega (p_1^2 - p_2^2) u \mathrm{d}x + \int_\Omega |\mathbf{q}| \mathrm{d}x, \\ \text{s.t.} \quad \mathbf{q} = \nabla u. \end{aligned}$$

Similarity, we have the following augmented Lagrangian function

$$\min_{u,\mathbf{q}} \max_{\xi} \mathcal{L}_u(u, \mathbf{q}; \xi_1) = \lambda \int_\Omega (p_1^2 - p_2^2) u \mathrm{d}x + \int_\Omega |\mathbf{q}| \mathrm{d}x - \int_\Omega \xi_1 (\mathbf{q} - \nabla u) \mathrm{d}x + \frac{r_1}{2} \int_\Omega (\mathbf{q} - \nabla u)^2 \mathrm{d}x.$$

where $\xi_1$ is the Lagrange multiplier, $r_1$ represents the penalty parameter. Convert the above problem into a sub-problem to solve. In the alternate optimization process, the optimization sub-problems of $u^{k+1}$ is

calculated respectively, and the auxiliary variables $\mathbf{q}^{k+1}$ and the Lagrangian multiplier $\xi_1^{k+1}$ are updated. Specifically, the formula is as follows

$$\begin{cases} u^{k+1} = \underset{u\in[0,1]}{\operatorname{argmin}} \mathcal{L}_u(u, \mathbf{q}^k; \xi_1^k), & \text{(19a)} \\ \mathbf{q}^{k+1} = \underset{\mathbf{q}}{\operatorname{argmin}} \mathcal{L}_u(u^{k+1}, \mathbf{q}; \xi_1^k), & \text{(19b)} \\ \xi_1^{k+1} = \xi_1^k - r_1(\mathbf{q}^{k+1} - \nabla u^{k+1}). & \text{(19c)} \end{cases}$$

• The subproblem (19a)

$$\min_{u\in[0,1]} \lambda \int_\Omega (p_1^2 - p_2^2)u\mathrm{d}x - \int_\Omega \xi_1^k(\mathbf{q}^k - \nabla u)\mathrm{d}x + \frac{r_1}{2}\int_\Omega (\mathbf{q}^k - \nabla u)^2\mathrm{d}x.$$

solving the following optimal equation

$$r_1\Delta u^{k+1} = \lambda(p_1^2 - p_2^2) + r_1\mathrm{div}(\mathbf{q}^k - \frac{\xi_1^k}{r_1}).$$

we can take the constraint by projecting $u$ on $[0, 1]$,

$$u_{i,j}^{k+1} = \min(\max(\mathcal{A}_{i,j}^{k+1}, 0), 1). \tag{20}$$

where

$$\mathcal{A}_{i,j}^{k+1} = \frac{1}{4}[(u_{i+1,j}^{k+1} + u_{i-1,j}^{k+1} + u_{i,j+1}^{k+1} + u_{i,j-1}^{k+1}) - \frac{\lambda(p_1^2 - p_2^2)}{r_1} + \mathrm{div}(\mathbf{q}^k - \frac{\xi_1^k}{r_1})].$$

and

$$\begin{aligned} \mathrm{div}(\mathbf{q}^k - \frac{\xi_1^k}{r_1}) = {} & \mathbf{q}_{i,j}^k + \mathbf{q}_{i-1,j}^k + \mathbf{q}_{i,j}^k + \mathbf{q}_{i,j-1}^k \\ & - \frac{1}{r_1}([\xi_1^k]_{i,j} + [\xi_1^k]_{i-1,j} + [\xi_1^k]_{i,j} + [\xi_1^k]_{i,j-1}). \end{aligned}$$

•The subproblem (19b)

$$\min_{\mathbf{q}} \int_\Omega |\mathbf{q}|\mathrm{d}x - \int_\Omega \xi_1^k(\mathbf{q} - \nabla u^{k+1})\mathrm{d}x + \frac{r_1}{2}\int_\Omega (\mathbf{q} - \nabla u^{k+1})^2\mathrm{d}x.$$

we use soft-threshold operator to solve $\mathbf{q}$.

$$\mathbf{q}^{k+1} = \mathrm{shrinkage}(\nabla u^{k+1} + \frac{\xi_1^k}{r_1}, \frac{1}{r_1}). \tag{21}$$

### 3.2 The $b_i, c_i$-subproblem

The ADMM method is a fast and efficient solution method. We formulate the minimization problem for $b_i, c_i$ as follows

$$\begin{aligned} \min_{b_1,b_2,c_1,c_2} \ & \lambda\int_\Omega p_1^2 u + p_2^2(1-u)\mathrm{d}x + \alpha\int_\Omega |\nabla b_1|^2\mathrm{d}x \\ & + \beta\int_\Omega |\nabla b_2|^2\mathrm{d}x + \nu\int_\Omega (b_1 - 1)^2\mathrm{d}x, \\ \text{s.t.} \quad & p_1 = I - b_1c_1 - b_2,\ p_2 = I - b_1c_2 - b_2. \end{aligned} \tag{22}$$

Based on augmented Lagrange method, we have the following formulation

$$\begin{aligned}\min_{b_1,b_2,p_1,p_2,c_1,c_2}\max_{\xi_2,\xi_3}\mathcal{L}(b_1,b_2,p_1,p_2,c_1,c_2;\xi_2,\xi_3) &= \lambda\int_\Omega p_1^2 u + p_2^2(1-u)\mathrm{dx}\\ &+\alpha\int_\Omega|\nabla b_1|^2\mathrm{dx}+\beta\int_\Omega|\nabla b_2|^2\mathrm{dx}+\nu\int_\Omega(b_1-1)^2\mathrm{dx}\\ &-\int_\Omega\xi_2(p_1-(I-b_1c_1-b_2))\mathrm{dx}+\frac{r_2}{2}\int_\Omega(p_1-(I-b_1c_1-b_2))^2\mathrm{dx}\\ &-\int_\Omega\xi_3(p_2-(I-b_1c_2-b_2))\mathrm{dx}+\frac{r_2}{2}\int_\Omega(p_2-(I-b_1c_2-b_2))^2\mathrm{dx}.\end{aligned}$$

where $\xi_2,\xi_3$ are the Lagrange multipliers, $r_2$ represents the penalty parameter. Convert the above problem into a sub-problem to solve.

$$\begin{cases} b_1^{k+1}=\underset{b_1}{\operatorname{argmin}}\,\mathcal{L}(b_1,b_2^k,p_1^k,p_2^k,c_1^k,c_2^k;\xi_2^k,\xi_3^k), & (23a)\\ b_2^{k+1}=\underset{b_2}{\operatorname{argmin}}\,\mathcal{L}(b_1^{k+1},b_2,p_1^k,p_2^k,c_1^k,c_2^k;\xi_2^k,\xi_3^k), & (23b)\\ p_1^{k+1}=\underset{p_1}{\operatorname{argmin}}\,\mathcal{L}(b_1^{k+1},b_2^{k+1},p_1,p_2^k,c_1^k,c_2^k;\xi_2^k,\xi_3^k), & (23c)\\ p_2^{k+1}=\underset{p_2}{\operatorname{argmin}}\,\mathcal{L}(b_1^{k+1},b_2^{k+1},p_1^{k+1},p_2,c_1^k,c_2^k;\xi_2^k,\xi_3^k), & (23d)\\ c_1^{k+1}=\underset{c_1}{\operatorname{argmin}}\,\mathcal{L}(b_1^{k+1},b_2^{k+1},p_1^{k+1},p_2^{k+1},c_1,c_2^k;\xi_2^k,\xi_3^k), & (23e)\\ c_2^{k+1}=\underset{c_2}{\operatorname{argmin}}\,\mathcal{L}(b_1^{k+1},b_2^{k+1},p_1^{k+1},p_2^{k+1},c_1^{k+1},c_2;\xi_2^k,\xi_3^k), & (23f)\\ \xi_2^{k+1}=\xi_2^k-r_2(p_1^{k+1}-(I-b_1^{k+1}c_1^{k+1}-b_2^{k+1})), & (23g)\\ \xi_3^{k+1}=\xi_3^k-r_2(p_2^{k+1}-(I-b_1^{k+1}c_2^{k+1}-b_2^{k+1})). & (23h)\end{cases}$$

•The subproblem (23a)

$$\begin{aligned}\min_{b_1}\ \alpha\int_\Omega|\nabla b_1|^2\mathrm{dx}+\frac{r_2}{2}\int_\Omega(p_1^k-(I-b_1c_1^k-b_2^k)-\frac{\xi_2^k}{r_2})^2\mathrm{dx}\\ +\nu\int_\Omega(b_1-1)^2\mathrm{dx}+\frac{r_2}{2}\int_\Omega(p_2^k-(I-b_1c_2^k-b_2^k)-\frac{\xi_3^k}{r_2})^2\mathrm{dx}.\end{aligned}$$

the Euler Lagrange formulation of $b_1$ can be written as

$$(-2\alpha\Delta+2\nu+r_2(c_1^k)^2+r_2(c_2^k)^2)b_1=r_2c_1^k(I-p_1^k-b_2^k+\frac{\xi_2^k}{r_2})+r_2c_2^k(I-p_2^k-b_2^k+\frac{\xi_3^k}{r_2})+2\nu\mathcal{I}$$

In periodic boundary conditions, we use the fast Fourier transform to solve the subproblem $b_1$

$$b_1^{k+1}=\mathcal{F}^{-1}\left(\frac{c_1^kr_2\mathcal{F}(I-p_1^k-b_2^k+\frac{\xi_2^k}{r_2})+c_2^kr_2\mathcal{F}(I-p_2^k-b_2^k+\frac{\xi_3^k}{r_2})+2\nu\mathcal{F}(\mathcal{I})}{(2\nu+r_2(c_1^k)^2+r_2(c_2^k)^2)\mathcal{F}(\mathcal{I})-2\alpha\mathcal{F}(\Delta)}\right). \quad (24)$$

•The subproblem (23b)

$$\begin{aligned}\min_{b_2}\beta\int_\Omega|\nabla b_2|^2\mathrm{dx}+\frac{r_2}{2}\int_\Omega(p_1^k-(I-b_1^{k+1}c_1^k-b_2)-\frac{\xi_2^k}{r_2})^2\mathrm{dx}\\ +\frac{r_2}{2}\int_\Omega(p_2^k-(I-b_1^{k+1}c_2^k-b_2)-\frac{\xi_3^k}{r_2})^2\mathrm{dx}.\end{aligned}$$

the Euler Lagrange formulation of $b_2$ can be represented as

$$(-2\beta\Delta + 2r_2)b_2 = r_2(I - p_1^k - b_1^{k+1}c_1^k + \frac{\xi_2^k}{r_2}) + r_2(I - p_2^k - b_1^{k+1}c_2^k + \frac{\xi_3^k}{r_2}).$$

In periodic boundary conditions, we use the fast Fourier transform to solve the subproblem $b_2$

$$b_2^{k+1} = \mathcal{F}^{-1}\left(\frac{r_2\mathcal{F}(I - p_1^k - b_1^{k+1}c_1^k + \frac{\xi_2^k}{r_2}) + r_2\mathcal{F}(I - p_2^k - b_1^{k+1}c_2^k + \frac{\xi_3^k}{r_2})}{2r_2\mathcal{F}(\mathcal{I}) - 2\beta\mathcal{F}(\Delta)}\right). \tag{25}$$

•The subproblem (23c)

$$\min_{p_1} \lambda \int_\Omega p_1^2 u \mathrm{dx} + \frac{r_2}{2}\int_\Omega (p_1 - (I - b_1^{k+1}c_1^k - b_2^{k+1}) - \frac{\xi_2^k}{r_2})^2 \mathrm{dx}.$$

The optimal solution to $p_1$ can be shown as

$$p_1^{k+1} = \frac{r_2(I - b_1^{k+1}c_1^k - b_2^{k+1}) + \xi_2^k}{2\lambda u + r_2}. \tag{26}$$

•The subproblem (23d)

$$\min_{p_2} \lambda \int_\Omega p_2^2 (1-u) \mathrm{dx} + \frac{r_2}{2}\int_\Omega (p_2 - (I - b_1^{k+1}c_2^k - b_2^{k+1}) - \frac{\xi_3^k}{r_2})^2 \mathrm{dx}.$$

The optimal solution to $p_2$ can be shown as

$$p_2^{k+1} = \frac{r_2(I - b_1^{k+1}c_2^k - b_2^{k+1}) + \xi_3^k}{2\lambda(1-u) + r_2}. \tag{27}$$

•The subproblem (23e)

$$\min_{c_1} \int_\Omega (p_1^{k+1} - (I - b_1^{k+1}c_1 - b_2^{k+1}) - \frac{\xi_2^k}{r_2})^2 \mathrm{dx}.$$

the optimal solution of variable $c_1$ gives

$$c_1^{k+1} = \frac{\int_\Omega b_1^{k+1}(I - b_2^{k+1} - p_1^{k+1} + \frac{\xi_2^k}{r_2})\mathrm{dx}}{\int_\Omega (b_1^{k+1})^2 \mathrm{dx}}. \tag{28}$$

•The subproblem (23f)

$$\min_{c_2} \int_\Omega (p_2^{k+1} - (I - b_1^{k+1}c_2 - b_2^{k+1}) - \frac{\xi_3^k}{r_2})^2 \mathrm{dx}.$$

similarly, the optimal solution of variable $c_2$ can be written as

$$c_2^{k+1} = \frac{\int_\Omega b_1^{k+1}(I - b_2^{k+1} - p_2^{k+1} + \frac{\xi_3^k}{r_2})\mathrm{dx}}{\int_\Omega (b_1^{k+1})^2 \mathrm{dx}}. \tag{29}$$

We choose the appropriate initial value to solve the problem iteratively, and the specific algorithm process is shown in Algorithm 1.

**Algorithm 1** The algorithm of the Multiplication-additive image segmentation model

Setting the initial values $u^0 = b_2^0 = p_1^0 = p_2^0 = c_1^0 = c_2^0 = \mathbf{q}^0 = \mathbf{0}$, $b_1^0 = \mathcal{I}$, the parameters $\lambda, \alpha, \beta > 0$, let $k = 1$ and start $k$-th iteration. Let $k = k + 1$ return to the $k + 1$ iteration till converge.

**while** (not converged and $k \leq K_{\max}$) **do**

- Compute $u^{k+1}$ from Eq.(20) by fixing other variables;
- $u_{i,j}^{k+1} = \min(\max(\mathcal{A}_{i,j}^{k+1}, 0), 1)$.
- where $\mathcal{A}_{i,j}^{k+1} = \frac{1}{4}[(u_{i+1,j}^{k+1} + u_{i-1,j}^{k+1} + u_{i,j+1}^{k+1} + u_{i,j-1}^{k+1}) - \frac{\lambda(p_1^2 - p_2^2)}{r_1} + \mathrm{div}(\mathbf{q}^k - \frac{\xi_1^k}{r_1})]$.
- Compute $\mathbf{q}^{k+1}$ from Eq.(21) by fixing other variables;
- $\mathbf{q}^{k+1} = \mathrm{shrinkage}(\nabla u^{k+1} + \frac{\xi_1^k}{r_1}, \frac{1}{r_1})$.
- Compute $b_1^{k+1}$ , $b_2^{k+1}$ from Eq.(24) and Eq.(25) by fixing other variables;
- $b_1^{k+1} = \mathcal{F}^{-1}\left(\frac{c_1^k r_2 \mathcal{F}(I - p_1^k - b_2^k + \frac{\xi_2^k}{r_2}) + c_2^k r_2 \mathcal{F}(I - p_2^k - b_2^k + \frac{\xi_3^k}{r_2}) + 2\nu\mathcal{F}(\mathcal{I})}{(2\nu + r_2(c_1^k)^2 + r_2(c_2^k)^2)\mathcal{F}(\mathcal{I}) - 2\alpha\mathcal{F}(\Delta)}\right)$.
- $b_2^{k+1} = \mathcal{F}^{-1}\left(\frac{r_2\mathcal{F}(I - p_1^k - b_1^{k+1}c_1^k + \frac{\xi_2^k}{r_2}) + r_2\mathcal{F}(I - p_2^k - b_1^{k+1}c_2^k + \frac{\xi_3^k}{r_2})}{2r_2\mathcal{F}(\mathcal{I}) - 2\beta\mathcal{F}(\Delta)}\right)$.
- Compute $p_1^{k+1}$, $p_2^{k+1}$ from Eq.(26) and Eq. (27) by fixing other variables;
- $p_1^{k+1} = \frac{r_2(I - b_1^{k+1}c_1^k - b_2^{k+1}) + \xi_2^k}{2\lambda u + r_2}$.
- $p_2^{k+1} = \frac{r_2(I - b_1^{k+1}c_2^k - b_2^{k+1}) + \xi_3^k}{2\lambda(1-u) + r_2}$.
- Compute $c_1^{k+1}$,$c_2^{k+1}$ from Eq. (28) and Eq. (29) by fixing other variables;
- $c_1^{k+1} = \dfrac{\int_\Omega b_1^{k+1}(I - b_2^{k+1} - p_1^{k+1} + \frac{\xi_2^k}{r_2})\mathrm{dx}}{\int_\Omega (b_1^{k+1})^2 \mathrm{dx}}$.
- $c_2^{k+1} = \dfrac{\int_\Omega b_1^{k+1}(I - b_2^{k+1} - p_2^{k+1} + \frac{\xi_3^k}{r_2})\mathrm{dx}}{\int_\Omega (b_1^{k+1})^2 \mathrm{dx}}$.
- Update $\xi_1^{k+1}$, $\xi_2^{k+1}$, $\xi_3^{k+1}$ from Eq.(19c), Eq. (23g), Eq. (23h);
- $\xi_1^{k+1} = \xi_1^k - r_1(\mathbf{q}^{k+1} - \nabla u^{k+1})$.
- $\xi_2^{k+1} = \xi_2^k - r_2(p_1^{k+1} - (I - b_1^{k+1}c_1^{k+1} - b_2^{k+1}))$,
- $\xi_3^{k+1} = \xi_3^k - r_2(p_2^{k+1} - (I - b_1^{k+1}c_2^{k+1} - b_2^{k+1}))$.

  Check the convergence condition $\frac{\|u^{k+1} - u^k\|_1}{\|u^k\|} \leq \epsilon$.

**end while**

Output result $u = u^{k+1}$.

## 4 Experimental results

### 4.1 Experiment introduction

To verify the feasibility and effectiveness of the model proposed in this paper, we conduct experiments on a variety of datasets including natural images, lesion segmentation, and images with noise. We have conducted comparative experiments with related segmentation models, such as ICTM [31], CVE [37], WBHMS [34], NLDA [9], LIC [16], L1PS [12]. All experiments are performed using MATLAB(R2021a) on a windows(10)(64bit) desktop computer with an Intel Core i7 3.20 GHz processor and 16.0GB of RAM.

### 4.2 Parameters setting

Throughout all experiments, we set the maximum number of iterations as $K_{\max} = 300$ and the termination condition error is $\epsilon = 10^{-4}$. The variables involved in our method are the data fidelity


**Fig. 2** Evaluation and comparison on natural images downloaded from the Weizmann segmentation dataset, and we label the images.

parameter $\lambda$, the weight of bias field $\alpha$, $\beta$, the penalty parameters $r_1$, $r_2$. The penalty parameter of the constraint term of multiplicative bias field $\nu$. The weight of the data fit term is $\lambda \in [4, 80]$. The range of $r_1$ and $r_2$ values are $r_1 \in [0.001, 2]$, $r_2 \in [0.001, 10]$ respectively. The range of weight parameter $\nu$ is $[0.01, 10]$. The range of the weight of bias field are $\alpha \in [10^2, 10^5]$, $\beta \in [10^2, 10^5]$ respectively. During the experiment, we adjust the parameters $\lambda$, $r_1$, $\alpha$ to achieve the ideal segmentation result. Other parameters are fixed at a certain value for different images. For different types of image segmentation tasks, we will again discuss the parameter range and its impact on the segmentation results separately.

Next, we represent the range of parameters involved in the comparative experiments. We refer to the corresponding literature and then adjust the parameters of the comparison method to the optimum to obtain the most ideal method results. The parameters involved are the regularization parameter, length item parameter, the penalty parameters, etc.

1) WBHMS: The detailed description of the WBHMS model is a weighted bounded Hessian variational model. The data fidelity parameter is chosen from $\lambda \in [0.4, 20]$, the penalty parameters $r_1$ and $r_2$ are chosen $r_1 \in [0.3, 20]$ and $r_2 \in [0.1, 8]$. the penalty parameter $r_3$ is chosen from $r_3 \in [0.005, 2]$, the value ranges of $c_1$ and $c_2$ are $c_1 \in [0.01, 0.45]$ and $r_2 \in [0.51, 0.90]$, respectively.
2) ICTM: The detailed description of the ICTM model is an efficient iterative thresholding method. The data fidelity parameter is chosen from $\lambda \in [0.02, 0.083]$, the time step $\delta \in [0, 0.1]$.
3) NLDA: The detailed description of the NLDA model is a new non-Lipschitz decomposition approach. The data fidelity parameter of $L_0$ are chosen from $\lambda \in [0.001, 0.3]$, the smooth term parameter is selected as $\alpha = 10^3$, the Tikhonov regular item parameter is set to $\gamma = 0.08$, and the penalty item parameter is set to $r = 10$.
4) LIC: The detailed description of the LIC model a local intensity clustering model. The data fidelity parameter is set to $\lambda = 1$, the length parameter is set to $\nu = 0.001 * 255 * 255$, the Gaussian kernel parameter is chosen to be $\sigma \in [15, 40]$, the level set regularization parameter is set to $\mu = 1$, the constant parameter in the Heaviside-Dirac function is set to $\varepsilon = 1$, the time step is set to $\delta = 0.1$.
5) L1PS: The detailed description of the L1PS model is a model with $L_1$ norm data fidelity term. The data fidelity term parameter is chosen as $\lambda \in [1, 10^3]$, the length term parameter is set as $\nu = 1$, the smooth term parameter is chosen as $\alpha \in \{2.5 * 10^5, 5 * 10^5\}$, the penalty parameter is set to $r_1 = \{10, 50\}, r_2 = \lambda$.
6) CVE: The detailed description of the CVE model is an Eulers elastica based Chan-Veses segmentation model. The parameter value $a$, $b$ of the function (10) in CVE [37] model are $a = 0.001$, $b \in [0.5, 6]$, the regular parameter $\eta \in [0.5, 6]$, the penalty parameters are $r_1 = 1$, $r_2 \in [0.5, 6]$, $r_3 \in [0.1, 0.5]$, $r_4 \in [0.8, 2]$.

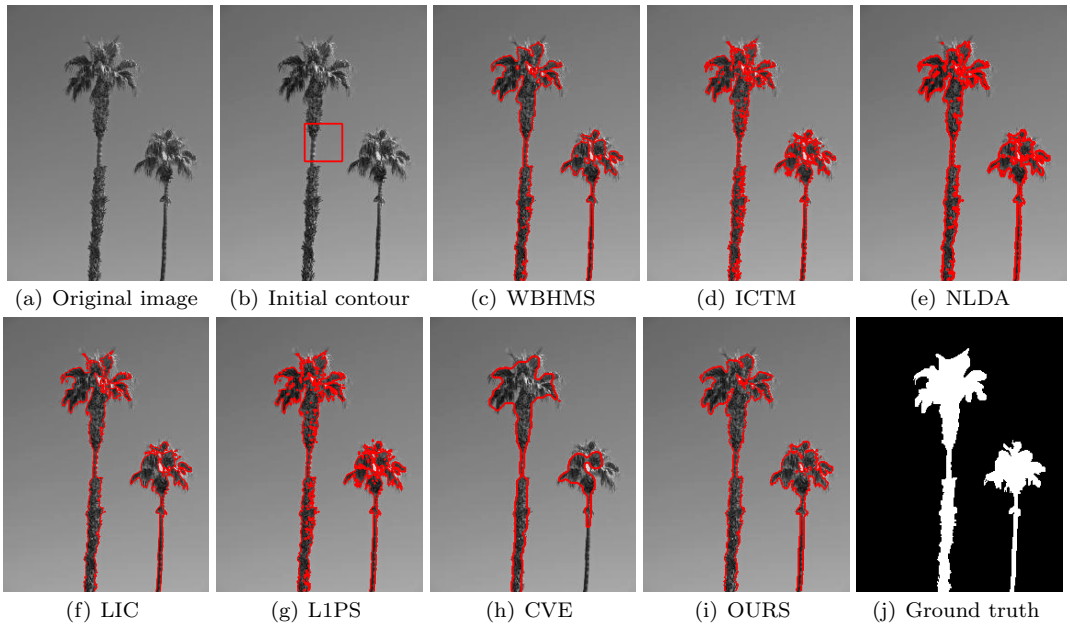

(a) Original image (b) Initial contour (c) WBHMS (d) ICTM (e) NLDA

(f) LIC (g) L1PS (h) CVE (i) OURS (j) Ground truth

**Fig. 3** Segmentation results of our and comparative models in natural image #9 are shown. (a): The original image 'rollingroscoe' is 300*255; (b): Initial contour of the image; (c)-(h): segmentation results of comparative models; (i) our segmentation result; (j): Ground truth.

### 4.3 Evaluation indicators

In the numerical experiment part, we use four metrics to objectively evaluate the segmentation results. For example, Jaccard Similarity (JS), Accuracy, F1-Score, Kappa coefficient ($\kappa$). In the literature [34], we can refer to the detailed explanation of each indicator. The closer the values of these indicators are to 1, the closer the experimental results are to the ground truth. Next, we discuss the influence of different images and parameters in the experiments on the results. Specifically, natural images, noise images, MRI images, etc.

### 4.4 Natural images

For the experimental operation, we set two termination criteria, one is the number of iterations, and the other is the relative error of the segmentation results. Next, we discuss the parameters of the model and the experimental results for different experimental datasets. The natural images on which we conduct related comparative experiments come from datasets on the web [1]. We arbitrarily select twelve images for related experiments, the indicator sets of Jaccard Similarity (JS), Accuracy, F1-Score, $\kappa$ are shown in Table 1. We present the comparative experimental results of images #9 and #11. Segmentation is challenging when the contrast between the target and the background is not obvious, or when the background is uneven. For images with a sharp contrast between the target area and the background, such as images #1, #4, #5, #7, etc. Whether it is our method or the comparison model, it can achieve a good segmentation effect. For images with similar image background and target, or images with noise, such as images #3, #11, etc. The experiment only needs to adjust parameter $\lambda$, $r_1$. The specific range are $\lambda \in [9, 12]$, $r_1 \in [0.001, 0.1]$. The range of other parameters can refer to those listed above.

[1] https://www.wisdom.weizmann.ac.il/ vision

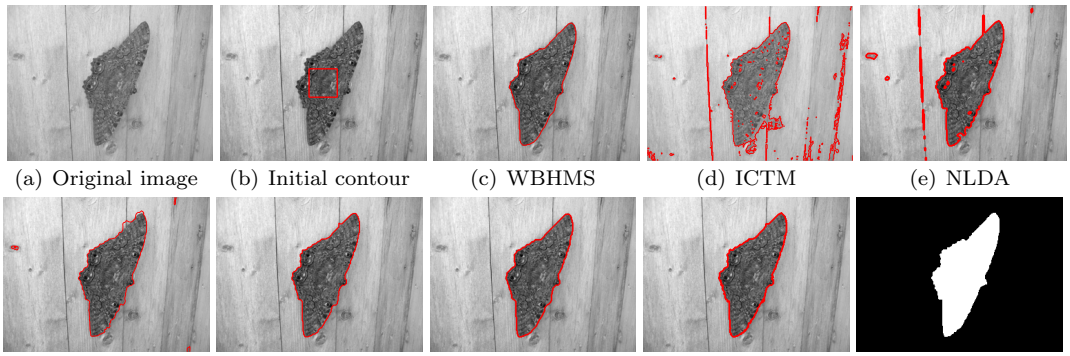

(a) Original image (b) Initial contour (c) WBHMS (d) ICTM (e) NLDA

(f) LIC (g) L1PS (h) CVE (i) OURS (j) Ground truth

**Fig. 4** Segmentation results of our and comparative models in natural image #10 are shown. (a): The original image 'butterfly' is 225*300; (b): Initial contour of the image; (c)-(h): segmentation results of comparative models; (i) our segmentation result; (j): Ground truth.

In Fig. 3, we focus on the details of the segmentation result image. Fig. 3(a) is the given image 'rollingroscoe'. Fig. 3(b) is an arbitrarily given initial contour. The initial contours of the experiments performed afterward are completely identical. Fig. 3(c)-3(h) are the segmentation results of the WBHMS, ICTM, NLDA, LIC, L1PS, and CVE models. From the experimental results, we can observe that these methods have over-segmentation or under-segmentation. The details of the upper leaves of the image 'rollingroscoe' are not handled properly. Fig. 3(i) is the experimental result of our method. Comparing our results with the ground-truth (Fig. 3(h)), our experimental results are the closest to the ideal segmentation results, both visually and on the index set. The parameters selection of the image are as follows, the weight of data fitting item $\lambda = 9$, the penalty values $r_1 = 0.004$, $r_2 = 7$. The value of $\nu$ is 0.01. The weight of multiplicative bias field and additive bias field are $\alpha = 10^2$, $\beta = 10^5$. The parameters $\alpha$ and $r_1$ have a great influence on the experimental results, and we can adjust these two parameters multiple times to obtain accurate results.

The image 'butterfly' is typical image with complex background. As shown in Fig.4, Fig. 4(a) is the given image 'butterfly'. Fig. 4(b) is an arbitrarily given initial contour. WBHMS, L1PS, and CVE models cannot identify the edge of image well and realize the segmentation of edge details. ICTM, LIC and NLDA models incorrectly segment the background information, similar to the interference of noise. The parameters of the image are selected as follows: the weight of data fitting item $\lambda = 9$, the values of $r_1$ and $r_2$ are $r_1 = 0.1$, $r_2 = 10$. The value of $\nu$ is 0.1. The weight of multiplicative bias field and additive bias field are $\alpha = 1 * 10^5$, $\beta = 10^3$.

To evaluate the segmentation results of our model under different initial contours, we conduct experiments on two natural images. The three natural images are #03, #07 and #10, respectively. We randomly selected six initial contours at different positions for experiments. In Fig.5, the initial contours are selected on the target or the background. The experimental results show the robustness of the proposed model to the initial conditions. The parameters selected for different initial profile experiments are shown below: For the image #03, we fixed the values of $r_1$ and $r_2$ are $r_1 = 1$, $r_2 = 9$. the weight of data fitting item $\lambda = 26$, The value of $\nu$ is 0.2. The values of $\alpha$ and $\beta$ are $\alpha = 1 * 10^5$, $\beta = 7 * 10^5$. For the image #07, the values of $r_1$ and $r_2$ are $r_1 = 0.002$, $r_2 = 10$. the weight of data fitting item $\lambda = 12$, The value of $\nu$ is 1. The values of $\alpha$ and $\beta$ are $\alpha = 1 * 10^5$, $\beta = 10^3$. For different initial contours, we just need to fine-tune and get the results we satisfied.

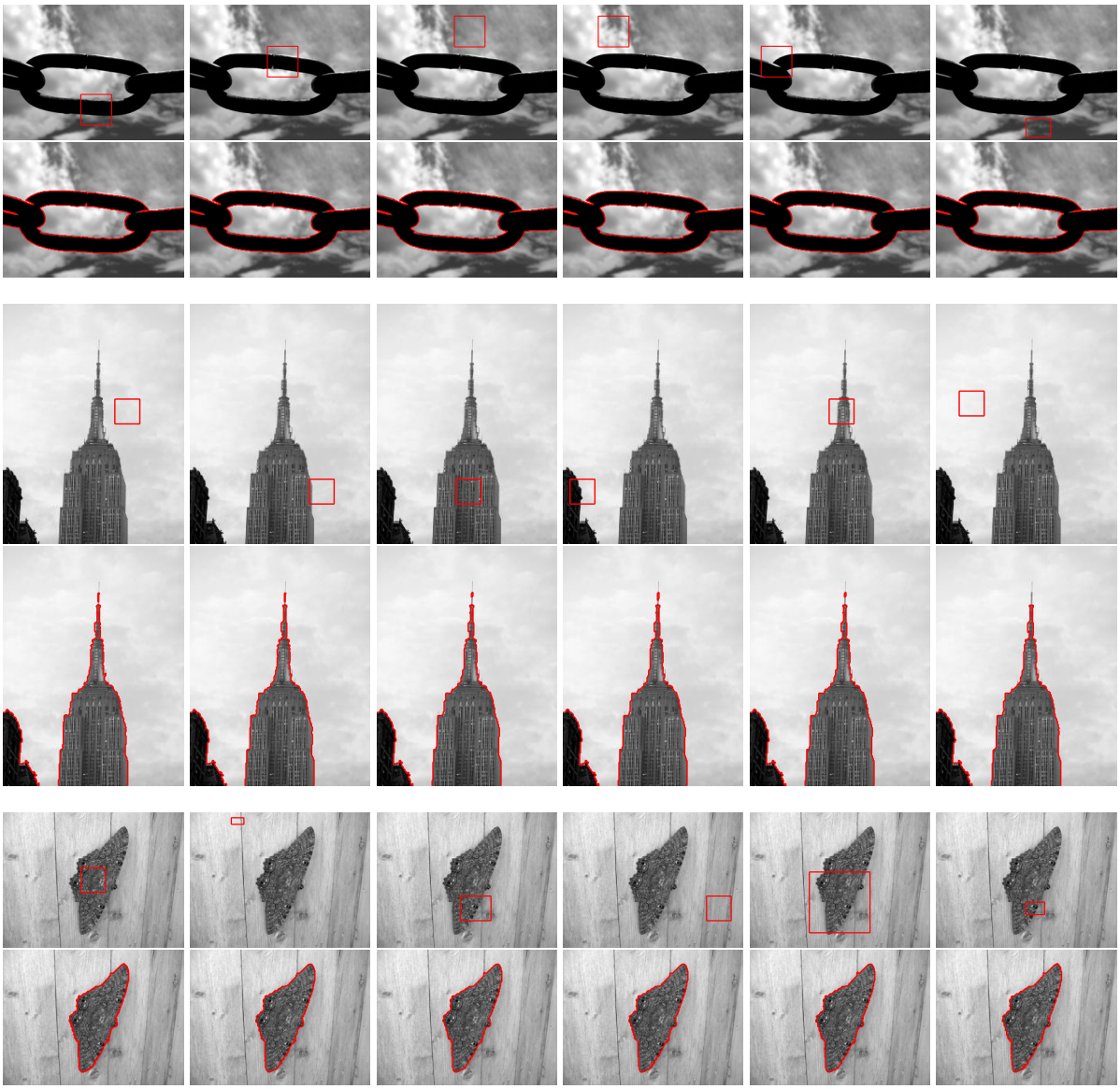

**Fig. 5** Evaluation and comparison on natural images #03, #07,#10, and we choose random initial contour of images and segmentation results.

### 4.5 MRI data

MRI has excellent imaging capabilities for soft tissue, with high resolution. Medically, MR imaging of the body is used to observe the catastrophe, liver, chest and other structures. Intensity inhomogeneity is how an artifact exists in MRI, along with random field noise, magnetization, and more. We conduct related medical image segmentation experiments on several MRI images from Henan Provincial People's Hospital. These images are approved by the Medical Ethics Committee of Henan Provincial People's Hospital. We ask experienced radiologists to perform manual segmentation as ground truth. Regarding the MRI experimental images, we focus on adjusting the parameters of the penalty function, and their specific value ranges are $r_1 \in [0.1, 2]$, $r_2 \in [0.001, 0.1]$. The segmentation experiment results of each

| Segmentation Evaluation Metrics for Natural Images | | | | | | | | | | | | | | |
|---|---|---|---|---|---|---|---|---|---|---|---|---|---|---|
| Criterions | JS | | | | | | | Accuracy | | | | | | |
| Images | WBHMS | ICTM | NLDA | LIC | L1PS | CVE | Ours | WBHMS | ICTM | NLDA | LIC | L1PS | CVE | OURS |
| #1 | 0.9545 | 0.9538 | 0.9839 | 0.9829 | 0.9818 | 0.9814 | 0.9831 | 0.9938 | 0.9937 | 0.9979 | 0.9978 | 0.9976 | 0.9976 | 0.9978 |
| #2 | 0.8398 | 0.8356 | 0.8439 | 0.8522 | 0.8450 | 0.8602 | 0.8612 | 0.9778 | 0.9773 | 0.9784 | 0.9795 | 0.9785 | 0.9798 | 0.9806 |
| #3 | 0.9131 | 0.6844 | 0.9268 | 0.9089 | 0.8803 | 0.8888 | 0.9185 | 0.9782 | 0.8935 | 0.9817 | 0.9771 | 0.9690 | 0.9723 | 0.9797 |
| #4 | 0.9929 | 0.9936 | 0.9939 | 0.9945 | 0.9946 | 0.9902 | 0.9946 | 0.9980 | 0.9982 | 0.9983 | 0.9984 | 0.9985 | 0.9972 | 0.9985 |
| #5 | 0.9718 | 0.9735 | 0.9736 | 0.9686 | 0.9734 | 0.9690 | 0.9751 | 0.9922 | 0.9927 | 0.9927 | 0.9913 | 0.9927 | 0.9914 | 0.9931 |
| #6 | 0.9098 | 0.9157 | 0.9311 | 0.9125 | 0.9244 | 0.9132 | 0.9304 | 0.9556 | 0.9585 | 0.9661 | 0.9572 | 0.9628 | 0.9563 | 0.9659 |
| #7 | 0.9645 | 0.9643 | 0.9676 | 0.9667 | 0.9675 | 0.9799 | 0.9717 | 0.9931 | 0.9930 | 0.9937 | 0.9935 | 0.9936 | 0.9961 | 0.9945 |
| #8 | 0.8110 | 0.7723 | 0.7971 | 0.8633 | 0.8979 | 0.8465 | 0.9103 | 0.9670 | 0.9602 | 0.9645 | 0.9761 | 0.9821 | 0.9729 | 0.9843 |
| #9 | 0.7541 | 0.6907 | 0.8434 | 0.7720 | 0.7443 | 0.7417 | 0.8737 | 0.9696 | 0.9617 | 0.9801 | 0.9717 | 0.9683 | 0.9671 | 0.9839 |
| #10 | 0.9438 | 0.7789 | 0.9401 | 0.9531 | 0.9697 | 0.9583 | 0.9734 | 0.9924 | 0.9635 | 0.9919 | 0.9936 | 0.9959 | 0.9944 | 0.9964 |
| #11 | 0.9254 | 0.7776 | 0.8910 | 0.8985 | 0.9251 | 0.9153 | 0.9574 | 0.9865 | 0.9515 | 0.9792 | 0.9819 | 0.9866 | 0.9846 | 0.9924 |
| #12 | 0.8867 | 0.7110 | 0.9404 | 0.4094 | 0.9073 | 0.8821 | 0.9433 | 0.9723 | 0.9298 | 0.9855 | 0.7132 | 0.9775 | 0.9711 | 0.9862 |
| *Mean* | 0.9056 | 0.8376 | 0.9194 | 0.8736 | 0.9169 | 0.9106 | **0.9411** | 0.9814 | 0.9645 | 0.9842 | 0.9609 | 0.9836 | 0.9817 | **0.9878** |
| *Std* | 0.0685 | 0.1121 | 0.0601 | 0.1528 | 0.0711 | 0.0697 | **0.0414** | 0.0127 | 0.0292 | 0.0108 | 0.0756 | 0.0119 | 0.0132 | **0.0092** |
| Criterions | F1-Score | | | | | | | $\kappa$ | | | | | | |
| Images | WBHMS | ICTM | NLDA | LIC | L1PS | CVE | Ours | WBHMS | ICTM | NLDA | LIC | L1PS | CVE | OURS |
| #1 | 0.9767 | 0.9764 | 0.9919 | 0.9914 | 0.9908 | 0.9906 | 0.9915 | 0.9732 | 0.9727 | 0.9907 | 0.9901 | 0.9895 | 0.9892 | 0.9902 |
| #2 | 0.9129 | 0.9104 | 0.9153 | 0.9202 | 0.9160 | 0.9248 | 0.9254 | 0.9003 | 0.8975 | 0.9030 | 0.9085 | 0.9037 | 0.9132 | 0.9143 |
| #3 | 0.9546 | 0.8126 | 0.9620 | 0.9523 | 0.9363 | 0.9411 | 0.9575 | 0.9402 | 0.7399 | 0.9500 | 0.9372 | 0.9159 | 0.9231 | 0.9442 |
| #4 | 0.9964 | 0.9968 | 0.9969 | 0.9973 | 0.9973 | 0.9951 | 0.9973 | 0.9950 | 0.9955 | 0.9957 | 0.9962 | 0.9962 | 0.9931 | 0.9962 |
| #5 | 0.9857 | 0.9866 | 0.9866 | 0.9840 | 0.9865 | 0.9843 | 0.9875 | 0.9803 | 0.9815 | 0.9816 | 0.9781 | 0.9815 | 0.9784 | 0.9828 |
| #6 | 0.9528 | 0.9560 | 0.9643 | 0.9542 | 0.9607 | 0.9546 | 0.9639 | 0.9110 | 0.9169 | 0.9321 | 0.9141 | 0.9255 | 0.9124 | 0.9316 |
| #7 | 0.9820 | 0.9518 | 0.9866 | 0.9831 | 0.9835 | 0.9899 | 0.9857 | 0.9777 | 0.9775 | 0.9816 | 0.9791 | 0.9795 | 0.9874 | 0.9822 |
| #8 | 0.8957 | 0.8715 | 0.8871 | 0.9266 | 0.9462 | 0.9168 | 0.9530 | 0.8763 | 0.8484 | 0.8664 | 0.9124 | 0.9356 | 0.9008 | 0.9436 |
| #9 | 0.8598 | 0.8171 | 0.9151 | 0.8713 | 0.8534 | 0.8517 | 0.9326 | 0.8431 | 0.7965 | 0.9039 | 0.8557 | 0.8360 | 0.8334 | 0.9235 |
| #10 | 0.9711 | 0.8757 | 0.9691 | 0.9760 | 0.9846 | 0.9754 | 0.9865 | 0.9667 | 0.8545 | 0.9645 | 0.9723 | 0.9823 | 0.9787 | 0.9845 |
| #11 | 0.9613 | 0.8749 | 0.9424 | 0.9466 | 0.9611 | 0.9558 | 0.9782 | 0.9531 | 0.8451 | 0.9296 | 0.9357 | 0.9530 | 0.9465 | 0.9736 |
| #12 | 0.9399 | 0.8311 | 0.9693 | 0.5810 | 0.9514 | 0.9373 | 0.9708 | 0.9220 | 0.7884 | 0.9598 | 0.3898 | 0.9368 | 0.9187 | 0.9618 |
| *Mean* | 0.9491 | 0.9051 | 0.9572 | 0.9237 | 0.9557 | 0.9515 | **0.9692** | 0.9366 | 0.8845 | 0.9466 | 0.8974 | 0.9446 | 0.9396 | **0.9607** |
| *Std* | 0.0391 | 0.0643 | 0.0336 | 0.1089 | 0.0388 | 0.0395 | **0.0223** | 0.0448 | 0.0822 | 0.0387 | 0.1582 | 0.0443 | 0.0462 | **0.0270** |
| Segmentation Evaluation Metrics for MRI Images | | | | | | | | | | | | | | |
| Criterions | JS | | | | | | | Accuracy | | | | | | |
| Images | WBHMS | ICTM | NLDA | LIC | L1PS | CVE | Ours | WBHMS | ICTM | NLDA | LIC | L1PS | CVE | OURS |
| *M*1 | 0.2022 | 0.7902 | 0.3012 | 0.1085 | 0.8723 | 0.3764 | 0.9498 | 0.8838 | 0.9928 | 0.9322 | 0.7538 | 0.9955 | 0.9520 | 0.9984 |
| *M*2 | 0.0420 | 0.0195 | 0.0091 | 0.0780 | 0.5526 | 0.2025 | 0.8608 | 0.9118 | 0.9198 | 0.0383 | 0.8961 | 0.9960 | 0.9786 | 0.9987 |
| *M*3 | 0.0367 | 0.0355 | 0.0360 | 0.0340 | 0.7800 | 0.0085 | 0.9277 | 0.9366 | 0.9449 | 0.9505 | 0.9308 | 0.9993 | 0.9138 | 0.9998 |
| *M*4 | 0.0045 | 0.0037 | 0.0052 | 0.0045 | 0.0041 | 0.0023 | 0.6650 | 0.8100 | 0.8692 | 0.8366 | 0.7840 | 0.8004 | 0.4476 | 0.9995 |
| *M*5 | 0.0432 | 0.0510 | 0.0091 | 0.0338 | 0.6022 | 0.0126 | 0.8789 | 0.8467 | 0.8643 | 0.1201 | 0.7968 | 0.9967 | 0.4376 | 0.9989 |
| *M*6 | 0.0347 | 0.0490 | 0.0318 | 0.0217 | 0.1819 | 0.0100 | 0.9260 | 0.9218 | 0.9544 | 0.9131 | 0.8586 | 0.9845 | 0.6499 | 0.9997 |
| *Mean* | 0.0606 | 0.1582 | 0.0654 | 0.0468 | 0.4989 | 0.1021 | **0.8680** | 0.8851 | 0.9242 | 0.6318 | 0.8367 | 0.9621 | 0.7299 | **0.9992** |
| *Std* | 0.0647 | 0.2831 | 0.1061 | 0.0354 | 0.3102 | 0.1417 | **0.0957** | 0.0444 | 0.0460 | 0.3931 | 0.0634 | 0.0725 | 0.2297 | **0.0005** |
| Criterions | F1-Score | | | | | | | $\kappa$ | | | | | | |
| Images | WBHMS | ICTM | NLDA | LIC | L1PS | CVE | Ours | WBHMS | ICTM | NLDA | LIC | L1PS | CVE | OURS |
| *M*1 | 0.3363 | 0.8828 | 0.4630 | 0.1958 | 0.9318 | 0.0569 | 0.9742 | 0.3005 | 0.8791 | 0.4365 | 0.1482 | 0.9295 | 0.5261 | 0.9734 |
| *M*2 | 0.0806 | 0.0382 | 0.0181 | 0.1446 | 0.7118 | 0.3368 | 0.9252 | 0.0655 | 0.0226 | 0.0005 | 0.1303 | 0.7100 | 0.3281 | 0.9245 |
| *M*3 | 0.0708 | 0.0686 | 0.0696 | 0.0658 | 0.8764 | 0.0168 | 0.9625 | 0.0658 | 0.0636 | 0.0646 | 0.0607 | 0.8760 | 0.0114 | 0.9624 |
| *M*4 | 0.0090 | 0.0073 | 0.0104 | 0.0089 | 0.0082 | 0.0046 | 0.7988 | 0.0062 | 0.0046 | 0.0077 | 0.0061 | 0.0055 | 0.0018 | 0.7986 |
| *M*5 | 0.0828 | 0.0970 | 0.0181 | 0.0655 | 0.7517 | 0.0248 | 0.9355 | 0.0684 | 0.0830 | 0.0020 | 0.0507 | 0.7501 | 0.0009 | 0.9350 |
| *M*6 | 0.0671 | 0.0933 | 0.0617 | 0.0424 | 0.3077 | 0.0198 | 0.9616 | 0.0608 | 0.0873 | 0.0552 | 0.0358 | 0.3036 | 0.0129 | 0.9614 |
| *Mean* | 0.1078 | 0.1979 | 0.1068 | 0.0872 | 0.5979 | 0.0766 | **0.9263** | 0.0945 | 0.1900 | 0.0944 | 0.0720 | 0.5958 | 0.1469 | **0.9259** |
| *Std* | 0.1052 | 0.3079 | 0.1609 | 0.0635 | 0.3311 | 0.1174 | **0.0594** | 0.0946 | 0.3096 | 0.1551 | 0.0507 | 0.3318 | 0.2063 | **0.0594** |

**Table 1** Metrics showing the segmentation results of our and comparative models in natural images and MRI images.

method of MRI are shown in Fig.6. All experiments use the same initial contour, but we find that several methods involved in the comparative experiments are not affected by the initial contour, such as WBHMS, CVE, etc. The experimental results show that the WBHMS, ICTM, NLDA, LIC and L1PS methods cannot segment the lesion area well, and segment other parts of the tissue incorrectly. Fig.7 is our method segmentation result. From top to bottom are the original image, the initial contour, our results, and the ground truth. The relevant indicator values are shown in Table 1. Our method has higher segmentation accuracy than other methods, and can intuitively see that the details are well segmented, as shown in Fig. 7.

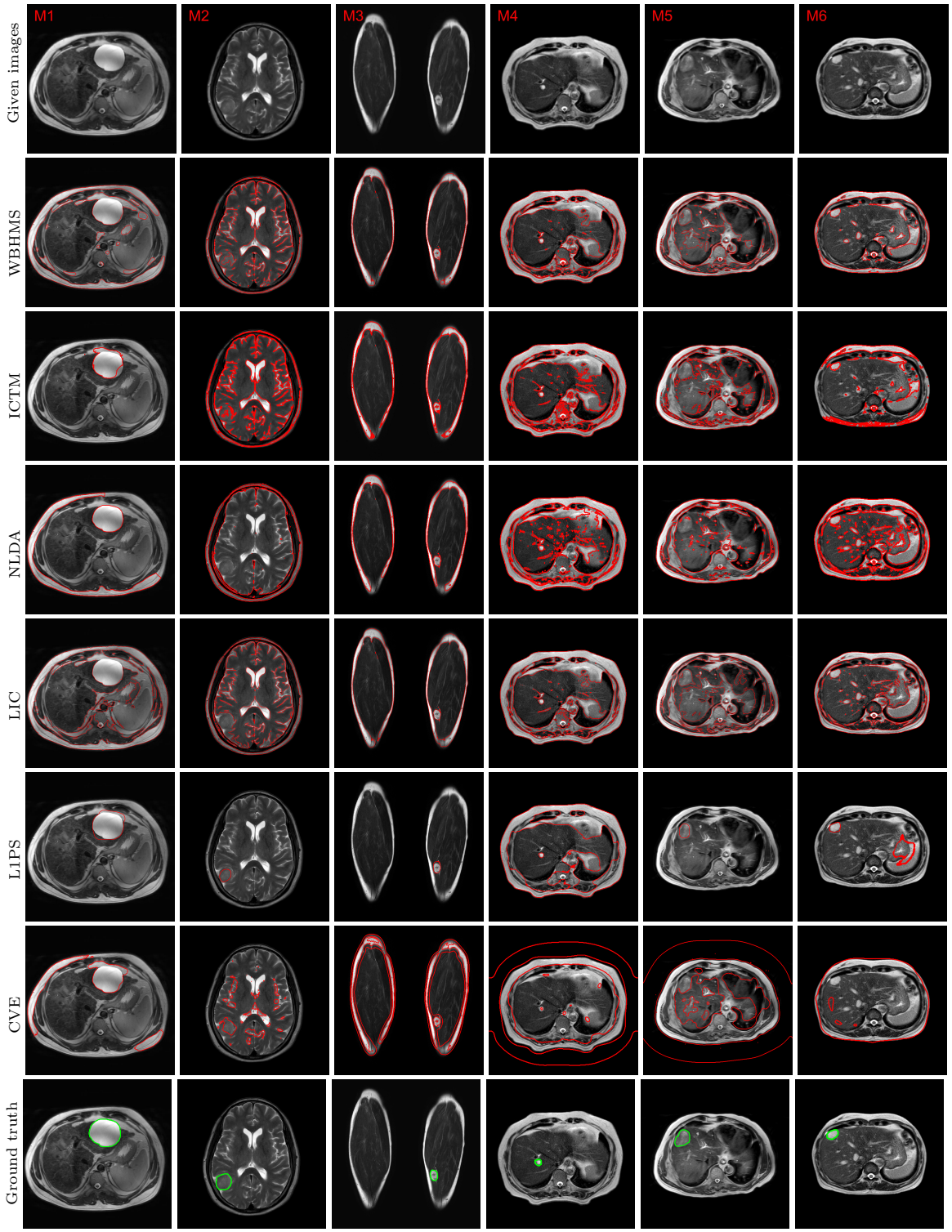


**Fig. 6** Segmentation results of our model in MRI images are shown. From top to bottom are the original image, the experimental results of the models WBHMS, ICTM, NLDA, LIC, L1PS, CVE, and the ground truth.

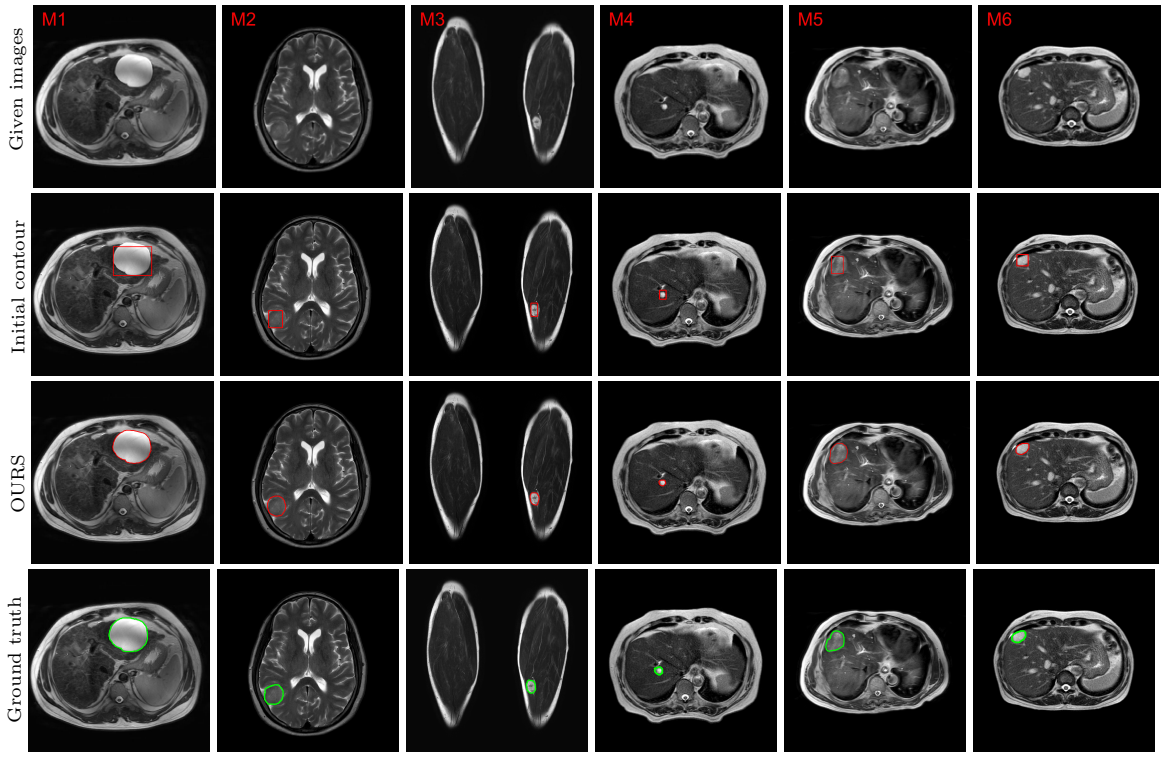


**Fig. 7** Segmentation results of our model in MRI images are shown. From top to bottom are the original image, the initial contour, our results, and the ground truth.

### 4.6 Noise images

The image size is "131*101" in Fig.8 shows a vascular X-ray image with uneven gray distribution. Due to the interference in the imaging process, the gray value of some vessels is lower than that of the background. In this case, image segmentation methods based on gray information often result in wrong segmentation results. The segmentation method based on the bias field model can solve this problem effectively. Our model can simultaneously segment and correct images with intensity inhomogeneous, and performs better in the segmentation of images with intensity inhomogeneous. We conduct experiments on several noisy images, where the initial contours are randomly selected. In Fig.8, Fig.8(a) are the given images, these images have varying degrees of noise and intensity inhomogeneity. We annotate the size of the image on the left side of the image. Fig.8(b) show the initial contour. Fig.8(c)-Fig.8(h) are the segmentation results for the models ICTM, CVE, WBHMS, NLDA, LIC, L1PS. It is observed from the experimental results that Models WBHMS, ICTM and CVE cannot correctly segment objects for images with uneven intensity. The ICTM model is sensitive to images with noise and cannot achieve correct segmentation. The NLDA, LIC and L1PS models cannot well describe the edge information of the target. Fig.8(i) are the segmentation result, which can accurately segment the sharp corners and edges of the images. For image segmentation with noise, the parameters of our model that we need to adjust are $\lambda$, $r_1$. The specific range is $\lambda \in [4, 11]$, $r_1 \in [0.001, 0.1]$. The range of other parameters can refer to the parameters listed above.

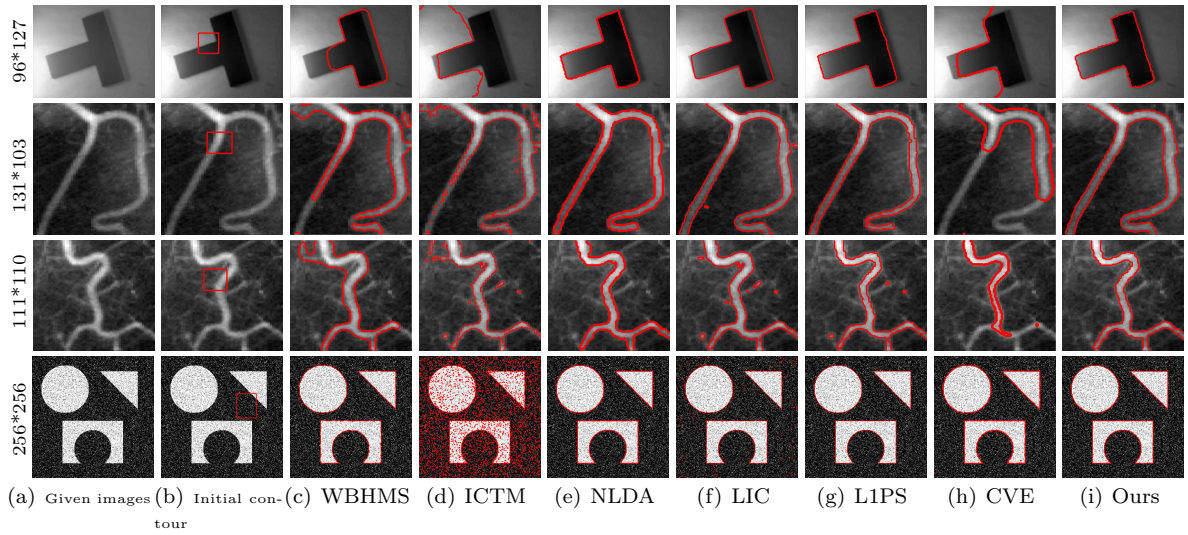


**Fig. 8** Segmentation results of our model under strong noise conditions. From left to right: original image and initial contour and segmentation result.

## 5 Conclusion

This paper proposed a new total variation model for bias field correction and segmentation. From the perspective of the bias field, there are two bias fields in the image, and they are corrected. Then we conducted a theoretical analysis of the model and conducted related comparative experiments on a wide range of experimental datasets, which fully demonstrate the effectiveness of our method. The experimental datasets include natural images, MRI images, and images with noise.

## References

1. Ali H, Badshah N, Chen K, Khan GA (2016) A variational model with hybrid images data fitting energies for segmentation of images with intensity inhomogeneity. Pattern Recognition 51:27–42
2. Ali H, Rada L, Badshah N (2018) Image segmentation for intensity inhomogeneity in presence of high noise. IEEE Transactions on Image Processing 27(8):3729–3738
3. Alirr OI (2020) Deep learning and level set approach for liver and tumor segmentation from ct scans. Journal of Applied Clinical Medical Physics 21(10):200–209
4. Caselles V, Kimmel R, Sapiro G (1997) Geodesic active contours. International journal of computer vision 22(1):61–79
5. Chan TF, Vese LA (2001) Active contours without edges. IEEE Transactions on image processing 10(2):266–277
6. Chan TF, Esedoglu S, Nikolova M (2006) Algorithms for finding global minimizers of image segmentation and denoising models. SIAM journal on applied mathematics 66(5):1632–1648
7. Duan Y, Chang H, Huang W, Zhou J, Lu Z, Wu C (2015) The $l\_\{0\}$ regularized mumford–shah model for bias correction and segmentation of medical images. IEEE Transactions on Image Processing 24(11):3927–3938
8. Gao S, Yang J, Yan Y (2012) A local modified chan–vese model for segmenting inhomogeneous multiphase images. International Journal of Imaging Systems and Technology 22(2):103–113
9. Guo X, Xue Y, Wu C (2021) Effective two-stage image segmentation: a new non-lipschitz decomposition approach with convergent algorithm. Journal of Mathematical Imaging and Vision 63(3):356–379

10. Horn BK (1974) Determining lightness from an image. Computer graphics and image processing 3(4):277–299
11. Jin Z, Wu Y, Min L, Ng MK (2020) A retinex-based total variation approach for image segmentation and bias correction. Applied Mathematical Modelling 79:52–67
12. Jung M (2017) Piecewise-smooth image segmentation models with $l_1$ data-fidelity terms. Journal of Scientific Computing 70(3):1229–1261
13. Kass M, Witkin A, Terzopoulos D (1988) Snakes: Active contour models. International journal of computer vision 1(4):321–331
14. Lai M (2015) Deep learning for medical image segmentation. arXiv preprint arXiv:150502000
15. Li C, Kao CY, Gore JC, Ding Z (2007) Implicit active contours driven by local binary fitting energy. In: 2007 IEEE Conference on Computer Vision and Pattern Recognition, IEEE, pp 1–7
16. Li C, Huang R, Ding Z, Gatenby JC, Metaxas DN, Gore JC (2011) A level set method for image segmentation in the presence of intensity inhomogeneities with application to mri. IEEE transactions on image processing 20(7):2007–2016
17. Li D, Chen S, Feng C, Li W, Yu K (2022) Bias correction of intensity inhomogeneous images hybridized with superpixel segmentation. Biomedical Signal Processing and Control 71:103207
18. Li F, Ng MK, Li C (2010) Variational fuzzy mumford–shah model for image segmentation. SIAM Journal on Applied Mathematics 70(7):2750–2770
19. Mahata N, Kahali S, Adhikari SK, Sing JK (2018) Local contextual information and gaussian function induced fuzzy clustering algorithm for brain mr image segmentation and intensity inhomogeneity estimation. Applied Soft Computing 68:586–596
20. Memon AA, Soomro S, Shahid MT, Munir A, Niaz A, Choi KN (2020) Segmentation of intensity-corrupted medical images using adaptive weight-based hybrid active contours. Computational and Mathematical Methods in Medicine 2020
21. Min H, Xia L, Han J, Wang X, Pan Q, Fu H, Wang H, Wong ST, Li H (2019) A multi-scale level set method based on local features for segmentation of images with intensity inhomogeneity. Pattern Recognition 91:69–85
22. Min L, Cui Q, Jin Z, Zeng T (2021) Inhomogeneous image segmentation based on local constant and global smoothness priors. Digital Signal Processing 111:102989
23. Mumford DB, Shah J (1989) Optimal approximations by piecewise smooth functions and associated variational problems. Communications on pure and applied mathematics
24. Niu Y, Cao J, Liu L, Guo H (2017) A novel acm for segmentation of medical image with intensity inhomogeneity. In: 2017 2nd IEEE International Conference on Computational Intelligence and Applications (ICCIA), IEEE, pp 308–311
25. Saman S, Narayanan SJ (2021) Active contour model driven by optimized energy functionals for mr brain tumor segmentation with intensity inhomogeneity correction. Multimedia Tools and Applications 80(14):21925–21954
26. Soomro S, Munir A, Choi KN (2018) Hybrid two-stage active contour method with region and edge information for intensity inhomogeneous image segmentation. PloS one 13(1):e0191827
27. Subudhi BN, Veerakumar T, Esakkirajan S, Ghosh A (2019) Context dependent fuzzy associated statistical model for intensity inhomogeneity correction from magnetic resonance images. IEEE Journal of Translational Engineering in Health and Medicine 7:1–9
28. Venkatesh V, Sharma N, Singh M (2020) Intensity inhomogeneity correction of mri images using inhomonet. Computerized Medical Imaging and Graphics 84:101748
29. Vese LA, Chan TF (2002) A multiphase level set framework for image segmentation using the mumford and shah model. International journal of computer vision 50(3):271–293
30. Vogel CR (2002) Computational methods for inverse problems. SIAM
31. Wang D, Li H, Wei X, Wang XP (2017) An efficient iterative thresholding method for image segmentation. Journal of Computational Physics 350:657–667

32. Wang XF, Huang DS, Xu H (2010) An efficient local chan–vese model for image segmentation. Pattern Recognition 43(3):603–618
33. Weng G, Dong B, Lei Y (2021) A level set method based on additive bias correction for image segmentation. Expert Systems with Applications 185:115633
34. Yang Y, Zhong Q, Duan Y, Zeng T (2020) A weighted bounded hessian variational model for image labeling and segmentation. Signal Processing 173:107564
35. Yu H, He F, Pan Y (2019) A novel segmentation model for medical images with intensity inhomogeneity based on adaptive perturbation. Multimedia Tools and Applications 78(9):11779–11798
36. Zhang K, Zhang L, Lam KM, Zhang D (2015) A level set approach to image segmentation with intensity inhomogeneity. IEEE transactions on cybernetics 46(2):546–557
37. Zhu W, Tai XC, Chan T (2013) Image segmentation using eulers elastica as the regularization. Journal of scientific computing 57(2):414–438
38. Zosso D, An J, Stevick J, Takaki N, Weiss M, Slaughter LS, Cao HH, Weiss PS, Bertozzi AL (2017) Image segmentation with dynamic artifacts detection and bias correction. Inverse Problems and Imaging 11(3):577–600